PHYSICAL REVIEW B **68**, 174108 (2003)

Structure and motion of basal dislocations in silicon carbide

A. T. Blumenau*
School of Physics, University of Exeter, Exeter EX4 4QL, United Kingdom
and Department of Physics, Faculty of Science, Universität Paderborn, D-33098 Paderborn, Germany

C. J. Fall and R. Jones
School of Physics, University of Exeter, Exeter EX4 4QL, United Kingdom

S. Öberg
Department of Mathematics, University of Luleå, S90187, Luleå, Sweden

T. Frauenheim
Department of Physics, Faculty of Science, Universität Paderborn, D-33098 Paderborn, Germany

P. R. Briddon
Department of Physics, University of Newcastle, Newcastle upon Tyne NE1 7RU, United Kingdom

(Received 9 May 2003; revised manuscript received 25 August 2003; published 21 November 2003)

30° and 90° Shockley partial dislocations lying in $\{111\}$ and basal planes of cubic and hexagonal silicon carbide, respectively, are investigated theoretically. Density-functional-based tight-binding total-energy calculations are used to determine the core structure and energetics of the dislocations. In a second step their electronic structure is investigated using a pseudopotential method with a Gaussian basis set. Finally, the thermal activation barriers to glide motion of 30° and 90° Shockley partials are calculated in terms of a process involving the formation and migration of kinks along the dislocation line. The mechanism for enhanced dislocation movement observed under current injection conditions in bipolar silicon carbide devices is discussed.

DOI: 10.1103/PhysRevB.68.174108 PACS number(s): 61.72.Lk, 71.15.Nc, 71.55.−i

I. INTRODUCTION

As a wide band-gap semiconductor which can be easily grown and doped, and possesses a high-field strength against breakdown, silicon carbide (SiC) is a promising material for high-power, high-temperature, and high-frequency devices. The material can be grown in a variety of polytypes involving different stacking sequences of tetrahedra and the electronic gap ranges from 2.39 to 3.33 eV, depending on the polytype.[1] In device development, one emphasis lies on high-power diodes: Bipolar $6H$-SiC diodes have been reported with reverse breakdown voltages as high as 4.5 kV (Ref. 2) and more recently $4H$-SiC PiN diodes have shown reverse breakdown voltages >5 kV with capacities to transmit very high powers >100 MW. However, recent experiments have shown that SiC PiN diodes degrade during forward-biased operation of the device even at moderate current densities,[3–6] sometimes below 1 A/cm^2.[7] This degradation means a considerable drop in the forward voltage, rendering the device useless after few days of constant operation. The voltage drop in $4H$-SiC is accompanied by the formation, propagation, and growth of stacking faults of triangular and sometimes rhombic shape.[5] Very recently the stacking fault edges, which lie along $\langle 11\bar{2}0\rangle$ directions, were identified by means of transmission electron microscopy and x-ray topography to be Shockley partials with Burgers vectors of $\frac{1}{3}\langle 1\bar{1}00\rangle$.[7,8]

Since neither the mechanical stresses nor the temperature are high enough to overcome the barrier to glide motion of these Shockley partials, it has been suggested that a *recombination-enhanced dislocation glide* (REDG) mechanism is responsible for the observed effect. This REDG mechanism—first proposed by Weeks *et al.*[9] for defect reactions and later refined by Sumi[10]—requires nonradiative electron-hole recombination sites to lie along the dislocation line. Part of the energy released following recombination has then to be directed into the formation and migration of kinks at the dislocation which are then able to move at or near room temperatures.[11]

Optical emission microscopy (OEM) has been used[6] to reveal that expansion of stacking faults occurs under low injection current at raised temperatures. The spectral analysis of the emission suggests stacking faults emit around 2.8 eV while their mobile bounding partial dislocations emit at lower energies around 1.8 eV. The stacking fault emission is in reasonable agreement with recent theoretical calculations[12–14] which report stacking fault related bands around 0.2 eV below E_c in $4H$-SiC. The OEM experiments also show that the activation energy for partial glide motion under forward bias is as low as 0.27 eV (Ref. 6) and substantially lower than the estimated value of 2.5 eV obtained from the temperature dependence of the yield stress[15] or the brittle-to-ductile transition temperature.[6,16] This has been interpreted as evidence for a REDG mechanism and preliminary data suggest a nonradiative recombination center at ~ 2.2 eV located at or near the core of a mobile Shockley partial.[6]

TABLE I. Elastic properties of $3C$-SiC. The first three rows give the independent elastic constants c_{ij} of $3C$-SiC. Those values for the shear modulus μ and Poisson's ratio ν marked with an asterisk are calculated as Voigt averages following Ref. 28 or Ref. 29. All values are given in GPa, except for ν, which is dimensionless.

	DFTB ($3C$)	T[a] ($3C$)	ETB[b] ($3C$)	LMTO[c] ($3C$)	VFF[d] ($3C$)	Expt.[e] ($3C$)	Expt.[f] ($3C$)
c_{11}	487	420	363	420	428		390
c_{12}	218	120	209	126	165		142
c_{44}	232	260	149	287	246		256
μ	193*	216*	120*	231*	200	192	203*
ν	0.241*	0.130*	0.300*	0.116*	0.187	0.168	0.153*

[a] Semiempirical interatomic potentials [Tersoff (Ref. 30)].

[b] Empirical tight binding [Lee and Joannopoulos (Ref. 31)].

[c] Full-potential linear muffin-tin orbital [Lambrecht *et al.* (Ref. 32)].

[d] Valence force field approach [Mirgorodsky *et al.* (Ref. 33)].

[e] Data by Carnahan (Ref. 34).

[f] Data derived from sound velocities by Feldman *et al.* (Ref. 35).

Thermally activated dislocation motion in SiC has been discussed previously,[17,18] but exclusively for the 90° glide partial in $3C$-SiC. In this work the atomic and electronic structures of both 90° and 30° partials in $3C$ and $2H$-SiC are investigated as well as the energetics of their motion.

II. COMPUTATIONAL METHODS

We use a density-functional-based tight-binding (DFTB) approach to determine the dislocation core structures and to calculate the formation and migration energies of kinks.

In DFTB the electronic wave functions are approximated by a linear combination of atomic orbitals involving a minimal basis set of *s* and *p* orbitals. The overlap and two center Hamiltonian matrix elements are obtained from atom-centered valence electron orbitals and the superposition of neutral atomic potentials. Exchange and correlation contributions to the total energy as well as the ionic core-core repulsion are taken into account by a repulsive pair potential. The latter is obtained by a fit of the total energies to full density-theory functional (DFT) calculations carried out on reference systems (e.g., bulk Si, diamond, and SiC).

More details have been given previously.[19,20] The atomic structures investigated here are geometrically optimized using a conjugate gradient algorithm until the force acting on each atom is less than 5×10^{-3} eV/Å.

The DFTB method has recently been applied to model dislocation core structures and energies in diamond[21,22] and was found to give results in agreement with DFT pseudopotential calculations carried out using localized[23,24] and plane-wave basis sets.[25]

Although the DFTB method describes dislocation structures and energetics sufficiently well, the use of a minimal basis and the tight-binding approximation prevent a detailed treatment of the electronic structure of extended defects. Therefore, we determine the electronic properties with the AIMPRO code[23,24] where the full DFT Hamiltonian, incorporating Bachelet-Hamann-Schlüter pseudopotentials,[26] is diagonalized using a basis of atom-centered *s*, *p*, and *d* Gaussian orbitals.

III. THE ELASTIC PROPERTIES OF BULK SiC

Long-range elastic effects play a significant role in the energetics of extended defects such as dislocations and it is imperative to determine the accuracy by which DFTB can predict both the anisotropic and isotropic elastic constants of SiC.

It is known that the different polytypes have rather similar elastic properties. This is especially true among the hexagonal types and hence, for reasons of simplicity, the calculations here are restricted to $3C$ and $2H$: the latter being a representative of the hexagonal polytypes. It has the smallest unit cell of all hexagonal polytypes and hence is the easiest to treat. The independent elastic constants of $3C$- and $2H$-SiC were obtained by suitably deforming a conventional unit cell and calculating the changes to the total energy of the cell. The integration over the Brillouin zone was accomplished using a Monkhorst-Pack-optimized set of $3\times3\times3$ $\boldsymbol{k}$ points.[27] Tables I and II show the elastic constants for the cubic and the hexagonal polytype along with experimental and theoretical data derived previously.

Experimental data on elastic properties of $3C$-SiC shown in Table I are rather sparse but our calculated value for the isotropic shear modulus μ agrees well with experiment while the Poisson ratio ν is about 50% too large. This error can be traced to an overestimate of c_{12} which contrasts with the good agreement found for c_{11} and c_{44}. Fortunately, a large error in ν has a much smaller error, less than 17%, on the energies of dislocations [see Eq. (2) below]. The calculated elastic constants (Table I) compare reasonably with previous theoretical investigations.

Table II gives the calculated and observed elastic constants for $2H$-SiC along with data for the other common hexagonal polytypes $4H$- and $6H$-SiC. In this case c_{13} is overestimated although the other constants are in good

TABLE II. Elastic properties of hexagonal SiC. The first five rows give the independent elastic constants c_{ij} of the respective polytype. Those values for the shear modulus μ and Poisson's ratio ν marked with an asterisk are calculated as Voigt averages following Ref. 28 or Ref. 29. All values are given in GPa, except for ν, which is dimensionless.

	DFTB ($2H$)	VFF [a] ($2H$)	Expt. [b] ($6H$)	Expt. [c] ($4H$)	Expt. [c] ($6H$)	Expt. [d] ($4H/6H$)
c_{11}	563	520	502			501
c_{12}	193	145	95			111
c_{13}	140	89				52
c_{33}	672	585	565	605	565	553
c_{44}	162	170	169			163
μ	190*	201				194*
ν	0.242*	0.174	0.207	0.212	0.212	0.161*

[a] Valence force field approach [Mirgorodsky *et al.* (Ref. 33)].
[b] Data by Arlt and Schodder (Ref. 36), average of two measurements.
[c] Data derived from piezoelectric properties by Karmann *et al.* (Ref. 37).
[d] Brillouin scattering [Kamitani *et al.* (Ref. 38)].

agreement with experiment and with previous theoretical results. The calculated shear modulus agrees very well with experiments on the more common polytypes while the Poisson ratio is again overestimated by about 50%. Nevertheless, the experimental estimates of this parameter vary by about 30%. In fact the experimental determination of c_{13} seems to be a problem, and the only value given here is derived from measurements on only one particular sample.[38] In the same work, no major differences between the two hexagonal polytypes $4H$ and $6H$ could be found.

IV. STRAIGHT DISLOCATIONS

To model the core structure, energy and electronic structure of straight dislocations, we use a supercell-cluster hybrid approach. In this approach, a single dislocation is inserted into a silicon carbide cylinder. Atoms on the faceted surface— cut along low index crystallographic directions— are saturated with hydrogen to inhibit surface reconstruction and to avoid dangling bonds and related electronic gap states. The dislocation is aligned with the axis of the cylinder and periodic boundary conditions are imposed along this axis. The hybrid approach has the advantage of studying a single infinite dislocation whereas at least a pair of dislocations (a dipole) has to be embedded in a cell if periodic boundary conditions are imposed on all its faces. The hybrid approach then eliminates the interaction of dislocations in different cells. For compound semiconductors, however, the hybrid cell is not necessarily stoichiometric and hence might contain more atoms of one element than the other. A more detailed description of this hybrid model in comparison with pure cluster and supercell models can be found in Ref. 21.

As pointed out in the Introduction, the technologically relevant dislocations lie in the basal plane of SiC along $[11\bar{2}0]$ and are dissociated into the 30° and 90° Shockley (glide) partial dislocations which border intrinsic stacking faults. Hence the investigations presented here will be entirely restricted to those partials.

A. Core structures

The topological structures of cores of the 30° and 90° Shockley glide dislocations lying on $\{111\}$ planes in $3C$-SiC and the basal plane in H-SiC are identical. This follows as the local atomic environments are identical up to third-nearest neighbors. Whereas in $4H$ and $6H$-SiC, there are several choices of glide planes, this is not so in $3C$ and $2H$ material.[57] The cylinder dimensions were similar to previous studies on diamond.[21] Their average radii R_0 and lengths were $\sim 3.5a_0$ and $\sqrt{2}a_0$ (with $a_0 = 4.36$ Å as the cubic lattice constant), and each contains about 500 atoms with a typical composition $C_{220}Si_{220}H_{84}$. The cylinders were periodically repeated in a square lattice with lattice constant 160 Å, and $\boldsymbol{k}$-point sampling was restricted to Γ.

Each partial dislocation with an edge component in a binary compound semiconductor can exist in two variants depending on the atom type located at the termination of the inserted plane. Therefore, in this work starting structures for the partials were generated by dissociating a perfect 60° silicon-terminated glide and a carbon-terminated glide dislocation into a 30° and 90° glide partial each. The model is then cut in half separating the two partials.

Moreover, it has been found in both Si and diamond, that the energy of a 90° partial with a double period has either competitive energy or lower energy than the single-period structures.[21,25,39,40] The double-period structures are constructed by creating a double kink at alternate sites along the dislocation line and this certainly reflects a low formation energy for such kinks. Hence, in this work we have investigated 30° and single- and double-period reconstruction of the 90° partials with both C and Si cores. The relaxed structures projected both parallel and normal to the $\{111\}$ glide plane for $3C$-SiC are shown in Fig. 1. Those in $2H$-SiC are topologically identical.

(a),(d): The 30° *glide partial.* The 30° glide partial reconstructs forming a line of bonded atom pairs. As shown in Table III, the Si-Si reconstructed bond length in the Si partial has almost exactly the same bond length as in bulk silicon. However, the corresponding C-C core reconstructed bonds in the carbon core are stretched by 17% compared to bulk diamond.

(b),(e): The 90° *glide partial (single period).* In the single-period (SP) structure of the 90° glide partial, reconstruction bonds are formed which connect the faulted with the unfaulted region of the glide plane. In the silicon-terminated core these Si-Si bonds are of comparable length to bulk silicon. Just as at the 30° partial, the reconstruction bonds in the carbon core are very stretched (Table III).

(c),(f): The 90° *glide partial (double period).* This double-period (DP) structure is obtained from the single-period structure by introducing double kinks at alternating sites. This leads to two types of reconstruction bonds between like atoms—one of which lies in the faulted region and the other

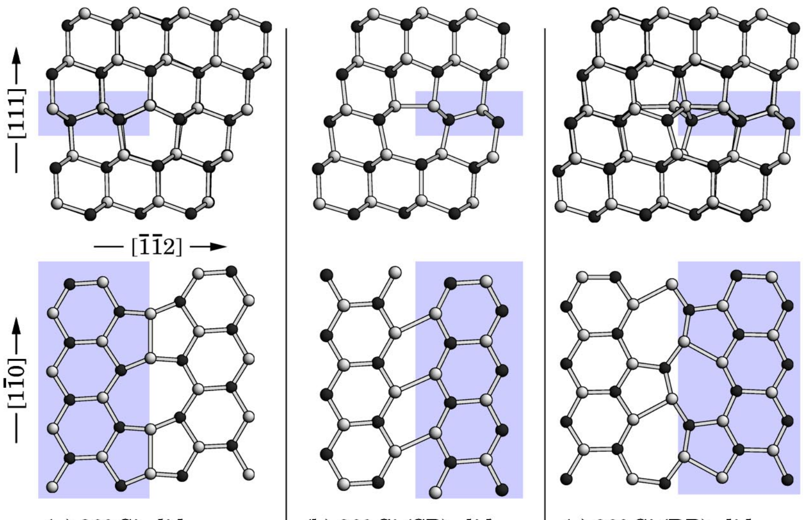

(a) 30° Si glide (b) 90° Si (SP) glide (c) 90° Si (DP) glide

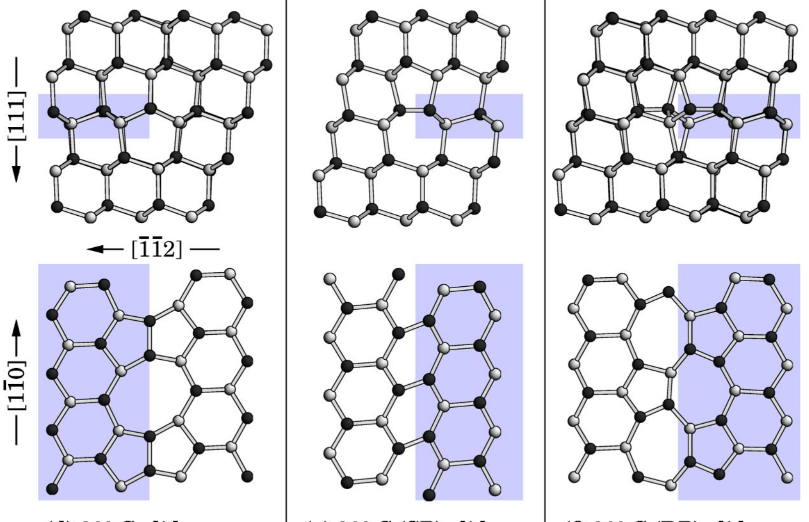

(d) 30° C glide (e) 90° C (SP) glide (f) 90° C (DP) glide

FIG. 1. The relaxed core structures of the Shockley partials in the $\{111\}$ plane of $3C$-SiC. (a)–(c) show the silicon-terminated partials. (d)–(f) show the carbon-terminated partials. For each structure, the upper figure shows a projection along the dislocation line while the lower figure shows the projection onto the (111) glide plane with the $[1\bar{1}0]$ dislocation line vertical in the figure. Carbon atoms are drawn in dark gray and silicon atoms in light gray. The region of the intrinsic stacking fault accompanying the partials is shaded. SP and DP denote the single-period and double-period core reconstruction for the 90° partials.

type in the unfaulted region. However, both types have nearly identical lengths. For both the silicon and the carbon core this results in a shortening of the reconstruction bonds, leaving the Si-Si bonds slightly compressed compared to bulk silicon. The C-C bonds, however, still appear to be about 10% stretched when compared with bulk diamond (Table III).

Identical calculations have been carried out for similar dislocations in $2H$-SiC. The structures differ from those of Fig. 1 only in that the intrinsic stacking fault now corresponds to an insertion of a plane with cubic stacking into wurtzite material. Hence, it is the unshaded areas in Fig. 1 which are faulted. The relaxed bond angles and lengths within the glide plane appear to be almost identical with those of cubic material. The largest deviation is found in the case of the carbon-terminated 90° (DP) partial where the C-C reconstructed bond length is marginally shorter, but still 9.3% longer than a C-C bond in diamond. This result supports the argument that the core structures of dislocations are very similar in all polytypes.

TABLE III. Fractional increase in bond lengths of reconstructed bonds relative to those in bulk material for Shockley glide partials in $3C$-SiC.

	30° glide (%)	90° (SP) glide (%)	90° (DP) glide (%)
Si-Si	$+0.7$	-0.4	-1.4
C-C	$+17.0$	$+14.6$	$+9.7$

B. Dislocation core energies

According to elasticity theory, the energy per unit length of a dislocation in a cylinder of radius R around a dislocation depends logarithmically on R and can be written as

$$E(R)=\frac{k(\beta)|\boldsymbol{b}|^2}{4\pi}\ln\left(\frac{R}{R_c}\right)+E_c, \quad R\geqslant R_c. \tag{1}$$

Here β is the angle between line direction and Burgers vector. This expression does not include the energy of the stacking fault associated with partial dislocations.

TABLE IV. The calculated energy factors $k(\beta)$ for 30° and 90° partials in cubic (C) and hexagonal SiC (H) found using isotropic (i) and anisotropic (a) elasticity theory. The first number is given by the DFT-based elastic constants obtained here, while the number in brackets is the factor obtained using the experimental constants based on Ref. 35 for 3C and Ref. 38 for 4H/6H summarized in Tables I and II.

		30°		90°	
		C	H	C	H
$k(\beta)^{(\mathrm{i})}$	(GPa)	208 (212)	205 (203)	254 (240)	251 (231)
$k(\beta)^{(\mathrm{a})}$	(GPa)	195 (191)	191 (191)	249 (231)	246 (227)

As continuum elasticity theory fails for distances of the order of interatomic distances, Eq. (1) holds only for radii larger than a core radius R_{c}. Hence the energy contained in the core, the so-called core energy E_{c}, cannot be obtained in elasticity theory but has to be determined through atomistic calculations. The energy factor $k(\beta)$ or the gradient of elastic energy versus $\ln(R/R_c)$ can be obtained from the elastic constants and the line direction and Burgers vector $\boldsymbol{b}$ of the dislocation. Using isotropic theory, $k(\beta)$ is given by[29]

$$k(\beta)^{(\mathrm{i})}=\mu\left(\cos^2\beta+\frac{\sin^2\beta}{1-\nu}\right). \tag{2}$$

In anisotropic elasticity theory $k(\beta)$ can be computed numerically.[29,41,42]

Table IV gives the energy factors obtained for the 30° and 90° partial dislocations in both 3C- and 2H-SiC, based on the DFTB elastic constants given above. For comparison, the values based on the experimental elastic constants for 3C and 4H/6H are shown in brackets. The differences between the energy factors in cubic and hexagonal stacking using either the experimental or theoretical elastic constants are very small, with those of wurtzite being slightly lower than the cubic values. The calculated values are within about 8% of the values found using the experimental elastic constants although it must be remembered there is some uncertainty in these. In comparison the energy factors found here are about half those found for the same structures in diamond[21] and certainly larger than those for silicon.

We now inquire how the energy factors and core energies and radii can be obtained entirely from atomistic (DFT-based) theory. To compare with Eq. (1), the DFTB total energy of perfect unstrained material is subtracted from the DFTB total energy of the dislocated model: It is a feature of the DFTB approximation that the energy E^i of individual atoms i can be obtained easily. The "formation energy" E_{f}^i of a particular atom in a structure is obtained by subtracting the total energy $E_{\mathrm{tot}}^{\mathrm{SiC}}(i)$ of the same type of atom in a perfect—and hence *stoichiometric*—SiC crystal:

$$E_{\mathrm{f}}^i=E_{\mathrm{tot}}^i-E_{\mathrm{tot}}^{\mathrm{SiC}}(i). \tag{3}$$

Nonstoichiometric growth conditions will result in chemical potentials different from $E_{\mathrm{tot}}^{\mathrm{SiC}}(i)$ and lead to different formation energies.[43]

The formation energy of the atoms in a cylinder surrounding the dislocation can now be written down and depends on the radius of the cylinder. To obtain the energy per unit length of a partial dislocation the energy γR of the stacking fault must be subtracted:

$$E_{\mathrm{f}}(R)=\frac{1}{L}\sum_{\mathcal{C}(R,L)}E_{\mathrm{f}}^i-\gamma R. \tag{4}$$

Here the sum is over all atoms in a cylinder $\mathcal{C}(R,L)$ of radius $R<R_0$ and of length L. R_0 is the radius of the cylinder whose surface is hydrogenated. Experimentally as well as theoretically intrinsic stacking fault energies are found to be of the order of only few mJ/m^2.[12,44–46] Therefore unlike in other semiconductors it does not play a major role in the glide motion of Shockley partial dislocations.

The variation of $E_{\mathrm{f}}(R)$ with cylinder radius R clearly displays logarithmic behavior at large R for all investigated partials. The core radii and core energies can be obtained by a fit of $E_{\mathrm{f}}(R)$ to Eq. (1). For $R\geqslant R_{\mathrm{c}}$ we obtain a linear dependence on $\ln(R)$ with a gradient proportional to the energy factor $k(\beta)$. Due to the discreteness of the spatial energy distribution, $E_{\mathrm{f}}(R)$ shows oscillations for small R, and R_{c} cannot be defined rigorously. For the 90° partial this has been demonstrated in Ref. 18. The energy factors, core radii, and core energies for all the Shockley partials in 3C- and 2H-SiC considered are given in Table V. One immediately sees that for all partials the energy factors obtained theoretically agree well with those found using elasticity theory and given in Table IV. On average the agreement is slightly better with anisotropic elasticity theory. We now discuss the core energies which cannot be derived from elasticity theory.

Silicon- and carbon-terminated partials. Compared with the Si-core structures, the corresponding C-core structures have a higher line energy: 380 meV/Å in the case of the 30° partials and around 580 meV/Å for the 90° partials. This probably reflects the dilated reconstruction bonds present in the carbon core and described above. However, as the atom projected formation energies will be affected by nonstoichiometric growth conditions, in carbon rich material the C-core structures might be the more stable partials. The core energies of carbon- and silicon-terminated partials will then be shifted with respect to each other according to the difference in chemical potentials.

Single- and double-period reconstructions. The Si-core double-period reconstruction of the 90° partial is found to be around 90 meV/Å lower in energy than the single-period structure. Similarly, the double-period carbon cores are more stable by about 100 meV/Å. For a length equal to a double period of about 6Å, this corresponds to about 0.6 eV. This

TABLE V. The calculated energy factors $k(\beta)$, core radii R_c, and core energies per unit length E_c of basal plane Shockley partials in stoichiometric SiC. The corresponding structures can be found in Fig. 1 for $3C$-SiC in the same sequence. To facilitate comparison between different dislocations with different core radii, the core energy E_c' corresponding to a radius of 6 Å is introduced.

		30° Si		90° Si (SP)		90° Si (DP)	
		$3C$	$2H$	$3C$	$2H$	$3C$	$2H$
$k(\beta)$ [a]	(GPa)	203	194	249	251	250	242
R_c	(Å)	5.3	5.5	3.9	3.4	6.0	5.2
E_c	(eV/Å)	0.44	0.45	0.51	0.46	0.59	0.54
E_c' (6 Å)	(eV/Å)	0.48	0.47	0.68	0.69	0.59	0.60
		30° C		90° C (SP)		90° C (DP)	
		$3C$	$2H$	$3C$	$2H$	$3C$	$2H$
$k(\beta)$ [a]	(GPa)	194	197	242	237	244	244
R_c	(Å)	4.5	4.7	5.0	4.1	4.7	4.1
E_c	(eV/Å)	0.77	0.78	1.20	1.13	1.08	1.02
E_c' (6 Å)	(eV/Å)	0.86	0.85	1.27	1.27	1.17	1.17

[a] Fit to $E_f(R)$ vs $\ln(R/R_c)$ plot for $R \geqslant R_c$ following Eq. (1).

energy difference is much greater than for similar partials in Si and about half of that found in diamond.[21,39]

Effects of the polytype. The core energies are almost independent of the polytype which is consistent with the absence of any pronounced influence on the elastic properties. This arises as the local bonding is identical up to the third shell of neighbors. Some differences occur in the core radii and core energies but the energies in cylinders of radius >6 Å are remarkably independent of the polytype.

C. The electronic structure of dislocation cores

Dislocations are line defects, periodic only along their line. Hence their electronic dispersion is described by a single $\boldsymbol{k}$ vector parallel to the dislocation line. To reveal the difference between the energy spectrum of the dislocation and the bulk the latter is projected onto this direction.

The band structures of the Shockley partials in $3C$- and $2H$-SiC are calculated using the DFT-pseudopotential code AIMPRO employing Gaussian basis sets. To reduce the computational effort, the band structures are obtained in smaller hybrid cells than those used above for the calculation of the core energies and contain on average about 120 atoms with $C_{50}Si_{50}H_{20}$ being a typical composition. The structures are relaxed, using a Monkhorst-Pack $2\times1\times1$ set of $\boldsymbol{k}$ points.[27] The projected electronic band structure of the relaxed structure is then calculated at 21 different $\boldsymbol{k}$ points along the dislocation axis.

Figure 2 shows the projected band structures of bulk $3C$- and $2H$-SiC as well as $2H$-SiC containing an intrinsic stacking fault. All band structures have been aligned at the valence-band maximum (VBM). The calculated width of the gap of bulk SiC is different from both experiment and the use of fully periodic boundary conditions in all three dimensions. Two competing effects have to be considered: An underestimate in the band gap caused by DFT and an opening of the gap caused by a confinement of the wave function to the H-terminated cylinder. Both effects compensate to some extent, and yield a gap 18% too small for both $3C$ and $2H$-SiC. The gap in the former polytype being 2.0 eV compared with 2.6 eV in the latter. This contrasts with a calculation using fully periodic boundary conditions where the gap is underestimated and values of 1.35 eV for $3C$ and 2.2 eV for $4H$ are found compared with experimental values of 2.39 and 3.26 eV, respectively.[1] The intrinsic stacking fault in $3C$-SiC does not introduce any deep electronic gap states in agreement with previous work by Käckell *et al.*[46] In $2H$-SiC however, an intrinsic fault represents a layer of cubic inclusion in the lattice, so one would anticipate localized gap states near the conduction-band minimum (CBM). Figure 3 shows these localized bands which reach ~0.5–0.6 eV below the CBM. In terms of energetic position and dispersion, these bands resemble the lowest conduction bands of the $3C$ polytype. Similar bands have been found by Miao

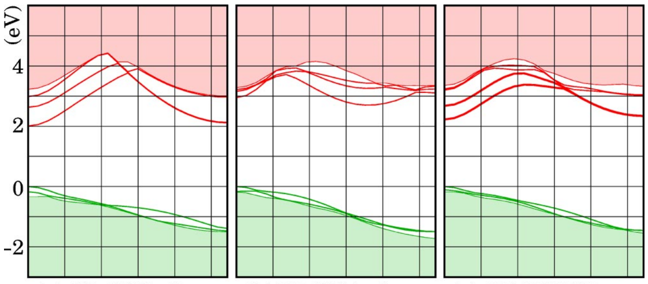

(a) $3C$–SiC bulk (b) $2H$–SiC bulk (c) $2H$–SiC ISF

FIG. 2. The band structures of bulk and faulted SiC in a hybrid (H-terminated) cylinder, projected onto the $\boldsymbol{k}$-space axis corresponding to the basal plane dislocation line direction ($[1\bar{1}0]$ in $3C$ and $[11\bar{2}0]$ in $2H$ with periodicities $a_0/\sqrt{2}$ and a_0, respectively). Only those bands which are close to the gap are drawn, and the regions above and below these bands are shaded. The origin of the Brillouin zone is at the far left of each band structure while the extreme right corresponds to $\boldsymbol{k}$ at the Brillouin-zone boundary.

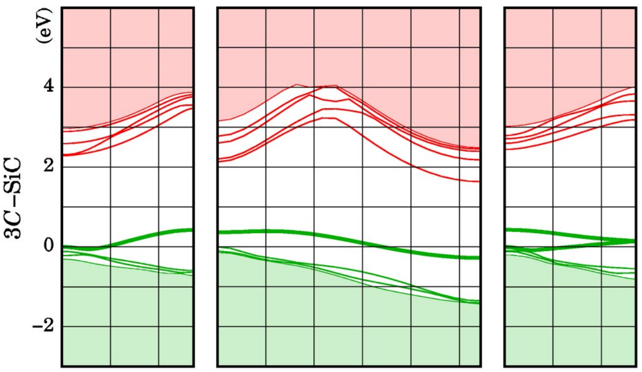

(a) 30° Si (b) 90° Si (SP) (c) 90° Si (DP)

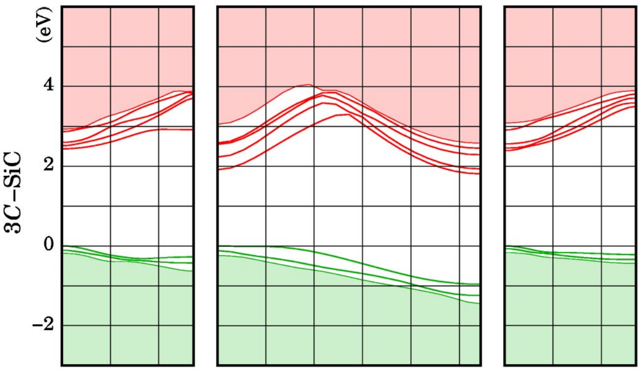

(d) 30° C (e) 90° C (SP) (f) 90° C (DP)

FIG. 3. The band structures of glide partials in $3C$-SiC projected onto the ***k***-space axis corresponding to the dislocation line direction $[1\overline{1}0]$ [with a periodicity length of $a_0/\sqrt{2}$ for (b) and (e) and $\sqrt{2}a_0$ for all others due to their double periodicity]. (a)–(c) show the band structures of the silicon-terminated partials and (d)–(f) show those of the carbon-terminated partials. Figure 1 gives the corresponding core structures in the same sequence.

et al.[12] for intrinsic faults in $4H$ ($\sim$0.3 eV below the CBM) and by Iwata *et al.*[13] in $4H$ and $6H$ ($\sim$0.2 eV below the CBM).

The projected band structures of the Shockley partials in $3C$-SiC are displayed in Fig. 3. It is immediately seen that none of the partials possesses midgap states reflecting the strength of the bond reconstruction along the cores. In a compound semiconductor such as SiC, however, the reconstruction bonds of the glide partials are of a different nature (Si-Si or C-C) compared to those in bulk material (Si-C). As can be seen in Fig. 3, only the silicon-terminated partials [(a)–(c)] appear to introduce deep occupied defect bands into the gap—reaching as far as 0.4 eV above the valence-band maximum. Analysis of the corresponding wave functions show that these states are strongly localized at the Si-Si reconstruction bonds. The 90° SP silicon partial introduces an empty band near the CBM but all other partials either leave the conduction edge unaffected or displace it slightly upwards. The slight variations in the width of the gap for the different partials result from differences in model geometry and size.

The equivalent band structures in $2H$-SiC are shown in Fig. 4. Near the valence band they are all almost identical with the corresponding ones in $3C$. Once again the Si partials lead to a occupied band about 0.4 eV above E_v. Near the conduction edge, only the 90° Si (SP) partial leads to deep gap state about 1 eV below E_c. The wider band gap found for the C (DP) and Si (DP) cores suggests that for these the core is less strained, thus explaining their lower core energy and stability over the SP structure.

V. THE ENERGETICS OF THERMALLY ACTIVATED DISLOCATION GLIDE

Glide motion arises from the effect of stress acting on the dislocation core. If the stress is insufficient to directly overcome the Peierls barrier, kinks must be generated by a thermal process and motion occurs by their migration along the dislocation line. Their formation energies E_f and migration barriers W_m then control the dislocation velocity in the absence of pinning centers or other obstacles. The dislocation mobility is activated with energy Q as

$$v_{\text{disl}} \propto e^{-Q/(kT)}. \tag{5}$$

Q is given as $Q=2E_f+W_m$ for short dislocation segments, and E_f+W_m for long segments.[29] The preexponential factors, which include entropy contributions, will not be calculated in this work. However they will be discussed qualitatively.

If there are several types of kinks, then the dislocation velocity will be controlled by those with the minimum of Q_L, Q_R, where Q_L, Q_R are the largest values of Q for kinks moving to the left or right respectively.

In the following the formation energy E_f and the kink migration barrier W_m will be determined for the 30° and 90° (SP) Shockley partials. The calculations, which are all performed using the DFTB method, are restricted to the cubic polytype as we have found above that all static properties of dislocations are unaffected by the polytype.

To avoid interaction of the kinks with their periodic images along the dislocation line, in this section the supercell-cluster hybrid model is abandoned in favor of pure cluster models.

A. The 90° SP partial dislocations

Figure 5 (far left panels) shows the relaxed kink structures at the 90° silicon and the 90° carbon single-period partial projected into the basal plane. All atoms are fourfold coordinated and within the glide plane, the structures of the left kink (not shown) and the right kink are identical when the different stacking on each side of the dislocation line is ignored. The difference in the reconstruction bond lengths of the two different partials (Si-Si or C-C bonds, respectively) leads to slightly different bond angles, but qualitatively both structures are very similar.

The kink formation energy E_f is obtained by comparing the energy of a cluster containing a straight dislocation segment with one of the same composition and containing a double kink. For the 90° (SP) partial, the cluster used extends over $6a_0/\sqrt{2}$ along the dislocation line and is composed as $C_{210}Si_{210}H_{214}$. This cluster size enables us to introduce a double kink with a kink-kink separation of $L=\sqrt{2}a_0$, while each kink remains $\sqrt{2}a_0$ from the surface.

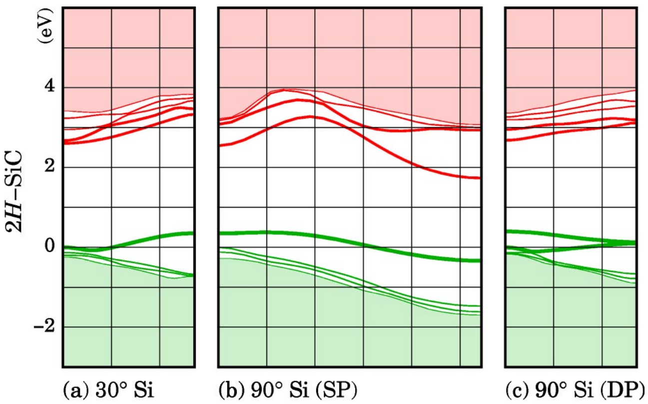

(a) 30° Si (b) 90° Si (SP) (c) 90° Si (DP)

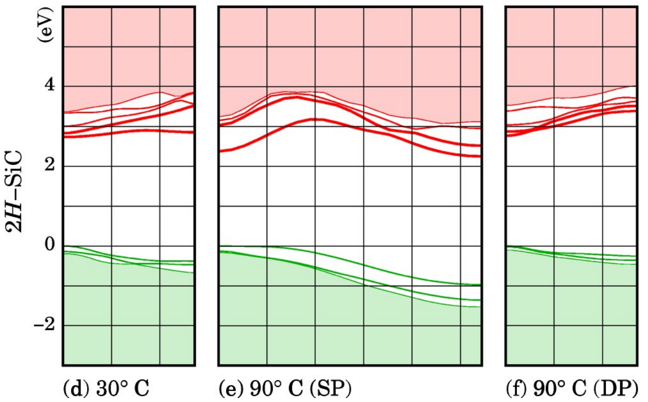

(d) 30° C (e) 90° C (SP) (f) 90° C (DP)

FIG. 4. The band structures of glide partials in $2H$-SiC projected onto the $\boldsymbol{k}$ axis parallel to the dislocation line direction $[11\bar{2}0]$ with periodicity a_0 for (b) and (e) and $2a_0$ for the remaining double-period partials. (a)–(c) show the band structures of the silicon-terminated partials and (d)–(f) show those of the carbon-terminated partials.

Assuming the formation energy of a single left kink and a single right kink to be the same and taking into account the energy of the faulted region generated along with the kinks, we obtain a double-kink formation energy:

$$2E_{\mathrm{f}}=E_{\mathrm{pair}}(L)-E_{\mathrm{LK,RK}}(L)-aL\gamma. \tag{6}$$

Here a is the kink height and $E_{\mathrm{LK,RK}}(L)$ the elastic kink-kink interaction energy of a 90° partial given by[29]

$$E_{\mathrm{LK,RK}}(L)=-\frac{\mu a^2}{8\pi L}\,\frac{1-2\nu}{1-\nu}\,|\boldsymbol{b}_{90}|^2. \tag{7}$$

The kink height $a=\sqrt{3/8}a_0$ is simply the separation of Peierls' valleys; for example, for the smallest possible double kink the interaction energy is found as $E_{\mathrm{LK,RK}}(L=a_0/\sqrt{2})\approx-0.24$ eV. Table VI gives the resulting single-kink formation energies for the silicon and the carbon partial and are each around 0.5 eV.

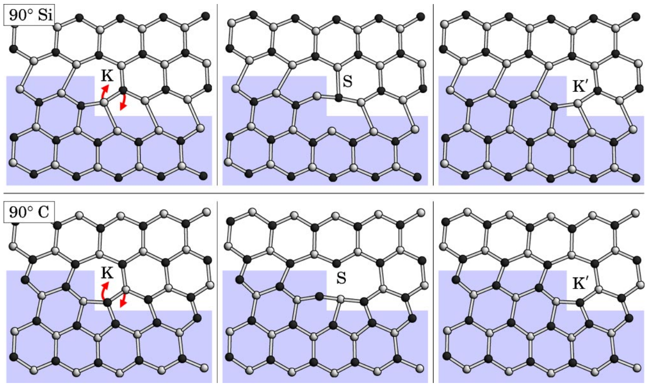

FIG. 5. Kink migration at the 90° (SP) glide partial. The relaxed structures of the starting kink K, the saddle point S, and the migrated kink K′ are shown projected into the glide plane. The faulted region is shaded and arrows indicate the movement of the two atoms mainly involved in kink migration. *Upper panel:* Silicon-terminated core. *Lower panel:* Carbon-terminated core.

An elementary kink migration step of the right kink is depicted in Fig. 5, where the initial configuration of the kink K, the saddle point S, and the displaced kink K′ are shown for both partials. In the process only two atoms are severely displaced breaking and forming new bonds. The motion of these two atoms—one silicon and one carbon atom—is used to characterize the migration step. Figure 6 shows the analysis for the motion of a single atom. Figure 7 (left) depicts the two-dimensional energy surface found when 10×10 intermediate points were used to model the migration of a single kink on the dislocation in the cluster. In the vicinity of the saddle point S, the parameter mesh is further refined by a factor of 10. The energy surfaces differ considerably for the two types of 90° partials. For the carbon partial the saddle point is well pronounced and the barrier can only be overcome by varying both parameters. The saddle-point configuration involves roughly equal displacements of the silicon and the carbon atom. For the silicon partial, however, the displacement of the carbon atom clearly dominates the path to the saddle point. This is displaced by 1.2 Å from the starting configuration, whereas the silicon atom moves only 0.6 Å. Also the different bonding situation for the two atoms will play a role: The movement of the Si atom involves the breaking and reforming of Si-Si bonds, which are rather "soft," whereas the movement of the C atom breaks and reforms "hard" Si-C bonds.

The calculations were repeated for the motion of a left kink. No difference in the migration barriers was found from the right kink described above. This reflects their similar structures. As can be seen in Table VI, the barrier to kink motion at the silicon-terminated partial is about 1 eV larger than that for a carbon-terminated partial. This might appear to be counterintuitive as the bonds in diamond are undoubtedly stronger than those in silicon. However one has to keep in mind that the C-C reconstruction bonds at the partial are stretched considerably when compared with diamond, and it is this effect which lowers the energy required to break the reconstructed bond necessary for kink migration.

From the kink formation energies and the migration barriers, the activation energy of the kink migration process can be evaluated following Eq. (5). Table VI gives the results. As the kink formation energies are almost the same at both partials, differences in the activation energy are due to differences in the kink migration barrier. Thus, when the glide of 90° partial dislocations is controlled by the formation and

TABLE VI. Single-kink formation energies E_f and migration barriers W_m for the 90° SP Shockley partials. The resulting thermal glide activation energy $Q_{90}=2E_f+W_m$ is relevant for short dislocation segments. The number in brackets gives the corresponding values or Q for long segments (E_f+W_m).

	90° (SP) glide		
	E_f	W_m	Q_{90}
Si	0.515	3.06	4.09 (3.58)
C	0.455	1.83	2.74 (2.29)

migration of kinks, i.e., when strong obstacles are not present, the carbon partial is clearly the more mobile. The kink formation and migration energies are schematically shown in Fig. 7 (right) for the first four steps involving an expansion of the kink pair. The dashed line connecting the minima represents schematically the formation energy of a double kink while the solid line includes the barriers necessary to be overcome for kink motion. The first few minima are considerably lower in energy due to an attractive interaction between the left and right kinks.

We remark here that broadly similar energies are expected for kink migration in the double-period structures and for other polytypes. This is because similar processes must occur in these cases.

B. The 30° partial dislocations

Due to the double periodicity present in the reconstructed 30° dislocation shown in Figs. 1(a) and 1(d), two varieties of left (LK1 and LK2) and right kinks (RK1 and RK2) occur. Figure 8 shows the different relaxed and reconstructed kink structures at the C-terminated partial. As can be seen, in the case of LK1 and RK1 the kink is located on a reconstruction bond, whereas in LK2 and RK2, the kinks are located between two reconstruction bonds. All atoms in these structures are fourfold coordinated suggesting relatively low kink formation energies.

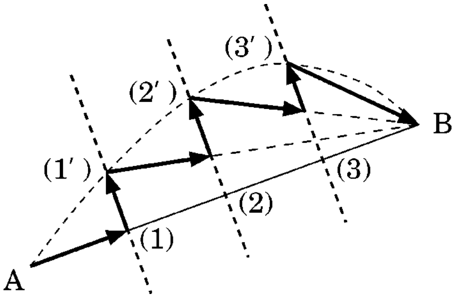

FIG. 6. Modeling the diffusion of a single atom. *A* and *B* are the positions of the moving atom in the starting and final relaxed structures, respectively. The motion of the atom is modeled as follows: Starting at A, the atom is sequentially displaced towards B. At each intermediate position, e.g. (1), the cluster is relaxed with a constraint that the mobile atom moves in a plane perpendicular to the line connecting (1) and B. The minimum energy is reached when the mobile atom lies at (1′). This process is then repeated until B is reached. The structural configurations corresponding to (1′), (2′), (3′), . . . lie on a low-energy path from A to B. The migration barrier corresponds with the greatest of these energies relative to the starting configuration. The method has been explained in detail in Ref. 47.

Table VII gives the energies for these kinks. The high-energy left kinks (LK2) appear with an interesting feature: The kink forms a reconstruction bond, which is of the opposite type to the reconstruction bonds of the respective partial—at the carbon-terminated partial with C-C reconstruction bonds the kink reconstructs with an "alien" Si-Si bond, and vice versa (Fig. 8).

In principle the structures at the silicon core and the carbon core are very similar, with only differences in bond lengths and angles due to the different character of the Si-Si and C-C bonds. Hence the kinks at the Si-terminated partial are not shown.

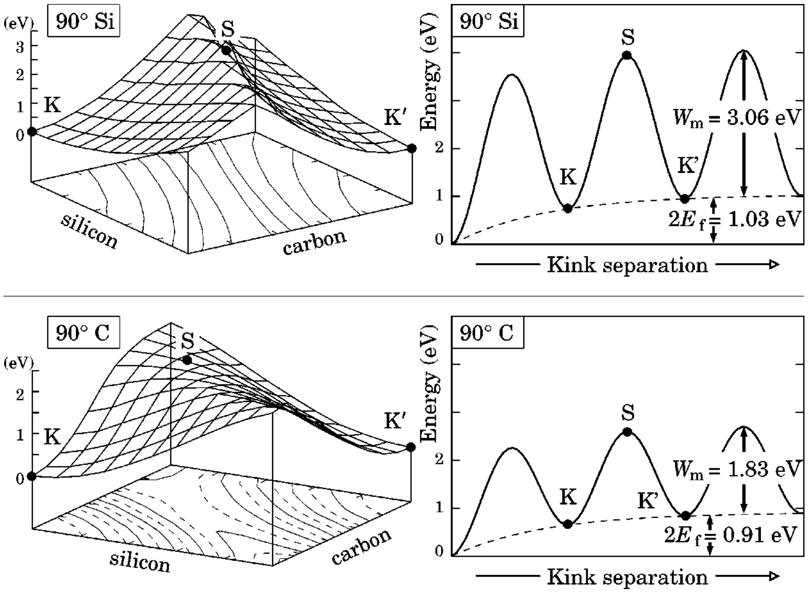

FIG. 7. The energies and barriers to kink formation and migration at the 90° (SP) glide partial. *Left diagrams:* The energy surface of the process leading from the starting kink K via the saddle point S to the migrated kink K′. The axes reflect the displacements of the carbon and silicon atom with arrows in Fig. 6. *Right diagrams:* Schematic representation of the energy barriers involved in the formation and migration of kinks. A kink pair is formed at K and subsequently expands to K′. S denotes saddle-point configuration. The dashed line connecting the minima represents the formation energy of the kink pair. *Upper panel:* Silicon-terminated core. *Lower panel:* Carbon-terminated core.

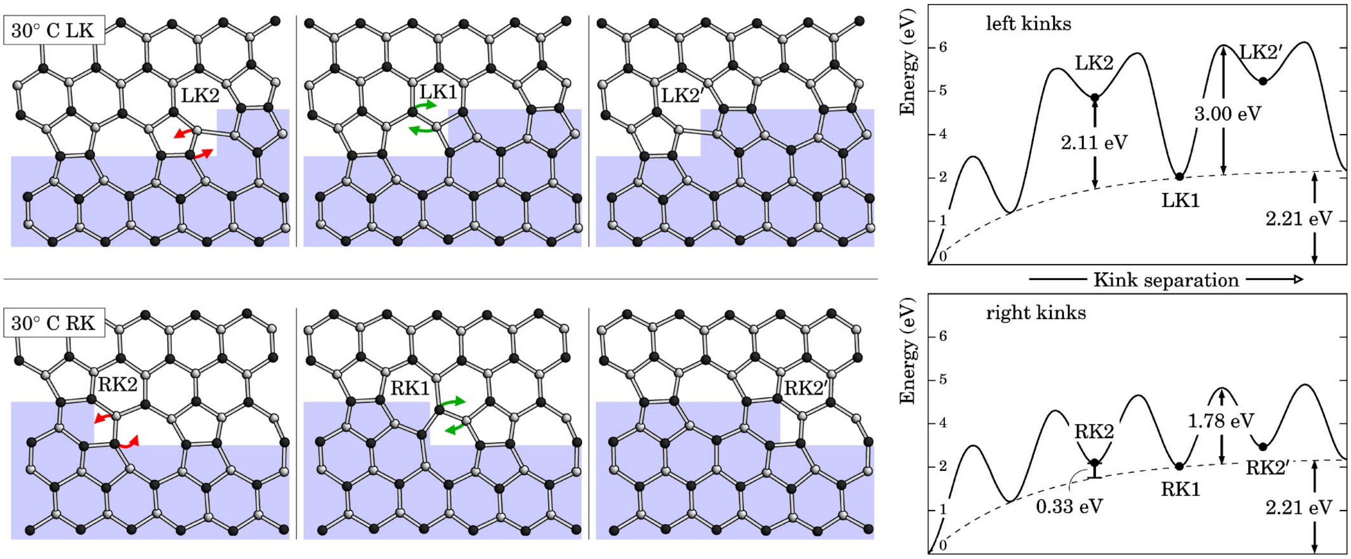

FIG. 8. The elementary migration steps of kinks at the 30° carbon partial: LK2→LK1→LK2′ (*upper panel*) and RK2→RK1→RK2′ (*lower panel*). The relaxed structures of the high-energy kinks LK2 and RK2, the low-energy kinks LK1 and RK1, and the extended high-energy kinks LK2′ and RK2′ are shown projected into the glide plane. The faulted region is shaded and arrows indicate the motion of the two involved atoms. The graphs on the right-hand side schematically represent the energy of the glide process: A kink pair is formed and subsequent migration of the two kinks enlarges their separation. The dashed line connecting the minima represents the formation energy of the kink pair.

The kink formation energies are obtained by introducing kink pairs on a dislocation embedded in a cluster in a similar way to that described in the last section. However, here the kink-kink interaction energy is given as[29]

$$E_{\mathrm{LK,RK}}(L) = -\frac{\mu a^2}{32\pi L}\,\frac{4+\nu}{1-\nu}\,|\boldsymbol{b}_{30}|^2. \qquad (8)$$

Compare with Eqs. (6) and (7). For the smallest possible double kink the interaction energy is found as $E_{\mathrm{LK,RK}}(L = a_0/\sqrt{2}) \approx -0.49$ eV. Since the structures of left and right kinks are very different, one cannot expect similar formation energies. Hence the single-kink energies are not individually found, but only the sum of two kink formation energies. We calculated the sum of formation energies for all possible four combinations of left with right kinks. The lowest energetic pair occurs for the LK1-RK1 with a formation energy: $2E_{\mathrm{f}}(1) = E_{\mathrm{f}}(\mathrm{LK1}) + E_{\mathrm{f}}(\mathrm{RK1})$. The energies of other combinations can be found by adding the appropriate Δ terms given in Table VII.

For right kinks RK2, Δ is small and around 0.3 eV. However, for left kinks, Δ is between 2 and 3 eV. The two right kinks appear with similar bond angle distortions, whereas among the two left kinks, it is clearly LK2 which shows the strongest distortions ($>20°$ for the two atoms closest to the kink). This could explain the large energy difference between LK1 and LK2.

As in the case of the 90° partial, the elementary migration steps are modeled in a cluster containing a dislocation with a single kink. Figure 8 shows the elementary kink migration steps LK2→LK1→LK2′ and RK2→RK1→RK2′ at the C-terminated partial. The resulting energy surfaces for each single step are very similar to those at the 90° partial shown in Fig. 7 and once again, for the silicon partial, it is the displacement of the carbon atom which dominates the process. Due to symmetry in the glide plane LK2→LK1 and LK1→LK2′ (or the equivalent right kink processes) are approximately symmetric processes and yield the same migration barriers within 1%. Table VII gives the resulting migration barriers W_{m} for both left and right kinks and Figs. 8 (right) and 9 schematically show the resulting energy of the migration processes of left and right kinks at each partial. Overall the right kinks are more mobile.

In principle, much of the discussion for the glide of the 90° partial applies to the 30°. However having two different barriers for left and right kink migrations respectively, results in a modified expression for the partial velocity. Equation (5) is replaced by[48]

TABLE VII. Kink formation energies E_{f} and migration barriers W_{m} for the 30° Shockley partials. The double periodicity implies two forms of left and right kinks (LK and RK). $2E_{\mathrm{f}}(1) = E_{\mathrm{f}}(\mathrm{LK1}) + E_{\mathrm{f}}(\mathrm{RK1})$ denotes the sum of the formation energies of the low-energy left and the low-energy right kink. $\Delta(\mathrm{LK})$ gives the energy difference between the low-energy (LK1) and the high-energy left kinks (LK2) and $\Delta(\mathrm{RK})$ denotes the same quantity for right kinks. To facilitate comparison with the 90° partials, an average activation energy $\overline{Q}_{30} = [2E_{\mathrm{f}}(\mathrm{LK1}) + W_{\mathrm{m}}(\mathrm{LK}) + 2E_{\mathrm{f}}(\mathrm{RK1}) + W_{\mathrm{m}}(\mathrm{RK})]/2$ is given. The glide activation energy assumes short dislocation segments and the values in brackets give the corresponding values for long segments.

	30° glide					
	$2E_{\mathrm{f}}(1)$	$\Delta(\mathrm{LK})$	$W_{\mathrm{m}}(\mathrm{LK})$	$\Delta(\mathrm{RK})$	$W_{\mathrm{m}}(\mathrm{RK})$	$\overline{Q}_{30}$
Si	1.62	2.87	3.79	0.28	2.87	4.95 (4.14)
C	2.21	2.11	3.00	0.33	1.78	4.60 (3.50)

$$v_{\mathrm{disl}} \propto e^{[-E_{\mathrm{f}}/(\mathrm{LK1})+E_{\mathrm{f}}(\mathrm{RK1})]kT}[e^{-W_{\mathrm{m}}(\mathrm{LK})/kT}+e^{-W_{\mathrm{m}}(\mathrm{RK})/kT}]. \tag{9}$$

Right kinks with their lower migration barrier dominate the glide process. However, to allow an easy comparison, as a crude approximation an average activation barrier $\overline{Q}_{30} = [2E_{\mathrm{f}}(\mathrm{LK1})+W_{\mathrm{m}}(\mathrm{LK})+2E_{\mathrm{f}}(\mathrm{RK1})+W_{\mathrm{m}}(\mathrm{RK})]/2$ can be defined for short segments. For long segments the same expression holds, however with half the formation energies. Both values are given in Table VII. Among the 30° partials the carbon core is slightly more mobile than the silicon-core partial, but the difference is less pronounced than for the 90° partial.

a. The influence of entropy effects. With small differences in activation energy between the Si- and C-terminated 30° partials (0.35- or 0.74-eV difference for short or long segments, respectively), entropy effects might play a major role when discussing glide motion. As mentioned earlier, in this work we will not explicitly calculate entropy contributions. To get an estimate however, we can compare with recent investigations of defect diffusion in SiC: For vacancy and antisite diffusion, total entropy contributions typically range from 0.1 to 0.4 eV at 1800 K.[49,50] Since differences in entropy between different diffusion processes then are smaller, we expect our results to be rather qualitatively independent of entropy effects. The carbon antisite is found to have a higher diffusivity than the silicon antisite, and this difference is even slightly enlarged if entropy is taken into account. As there are some similarities between kinks at C-terminated partials and carbon antisites (both possess C-C bonds), and equivalently between Si partials and silicon antisites, we would at least not expect a change in the order of dislocation mobilities due to entropy contributions.

b. Summary. In comparison, the 90° partial is the more mobile species. Further, the purely thermal mobility of carbon partials in the absence of strong obstacles appears to be higher than that of silicon partials, and the velocities of undecorated neutral partials are largely controlled by their kink migration energy.

In comparison with earlier DFT-based results for the 90° (SP) partials in SiC by Sitch *et al.*,[17] the kink migration barrier found here is about 0.4 eV higher at both the silicon and the carbon partial. This might result from the use of much larger cluster models in this work, which give a more accurate representation of the stress response of the surrounding bulk material. In addition, in Ref. 17 the migration barrier was deduced from the barrier to double-kink formation, rather than kink expansion as modeled here. The formation energy of the smallest double kink at the C partial also is 0.4 eV lower than that found in the present work. A more striking difference is found for the Si partial. In this work the kink formation energy appears to be similar to that at the C core, whereas in Ref. 17 it is negligible. Nevertheless, both calculations conclude that the thermal activation barrier for the carbon partial is lower than that of the silicon partial.

C. Influence of kinks on the electronic structure

The question now arises if any additional electronic levels are introduced in the band gap due to the presence of kinks. Once again finite hydrogenated clusters containing a single kink on various glide dislocations in $3C$-SiC are investigated. The cluster stoichiometries are $\mathrm{Si_{94}C_{89}H_{128}}$ (straight 30° Si), $\mathrm{Si_{94}C_{89}H_{124}}$ (left kinks in 30° Si), $\mathrm{Si_{110}C_{103}H_{142}}$ (right kinks in 30° Si), and $\mathrm{Si_{125}C_{125}H_{150}}$ (straight and kinked 90° partials). The 30° carbon clusters are constructed by simply swapping Si and C.

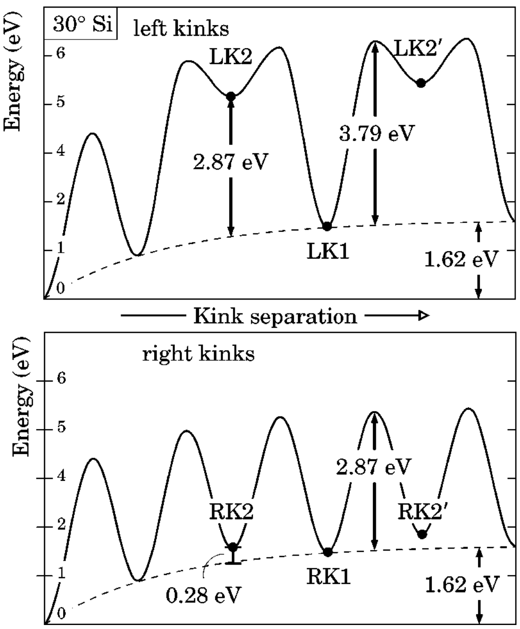

FIG. 9. The energies and barriers to kink formation and migration at the 30° Si glide partial. Schematic representation of the energetics of the glide process. For further details see caption of Fig. 8.

The structures are relaxed using AIMPRO and their resulting electronic Kohn-Sham eigenvalue spectra are given in Figs. 10 and 11. The electronic band gaps obtained vary due to the differences in cluster size and geometry for the different types of partials and kinks. As a general observation for both 30° partials, the high-energy kinks (LK2 and RK2) give rise to a slightly more pronounced local gap narrowing than their low-energy counterparts (LK1 and RK1). This can probably be interpreted as a consequence of the larger strain field associated with LK2 and RK2.

In the case of the silicon-terminated 30° and 90° partials the highest occupied gap levels, $\sim E_v + 0.2$ eV, are localized on the Si-Si reconstruction bonds. These characteristic levels correspond to the Si-Si related band above the VBM found in the band structures of infinite Si-terminated partials given earlier (Figs. 3 and 4). Most kink structures in carbon-terminated partials do not lead to additional gap levels. Only three kink structures show more outstanding electronic characteristics.

30° Si *LK2.* Here the highest occupied level is pushed $\sim$0.4 eV into the band gap. This effect is possibly related to the local strain at the kink structure.

30° C *LK2.* A feature common to all silicon-terminated partials can also be found in the carbon-terminated LK2 structure: As shown in Fig. 8, this is the only kink in a C-terminated partial which appears with an ‘‘alien’’ Si-Si reconstruction bond. It is this bond which in the neutral charge state gives rise to the occupied gap level close to the VBM—very similar to what is found for the Si partials.

30° C *RK1*. This kink reconstructs with a considerable bond angle distortion which appears to give rise to the empty level observed in the upper half of the gap.

VI. SUMMARY AND CONCLUSIONS

Generally speaking, the core reconstructions of partial dislocations in the basal plane of SiC are very similar to those found in earlier work for diamond.[21] Unlike in diamond though, in SiC one has to distinguish between two types of core reconstructions for each dislocation: Silicon-terminated and carbon-terminated cores with Si-Si and C-C reconstruction bonds, respectively.

In all the structures investigated, the Si-Si core bonds are of comparable length to bonds in bulk Si. The C-C bonds of the carbon-terminated cores, however, are all stretched by $\approx 15\%$ compared with the carbon bond length in diamond. As a consequence the carbon-terminated cores possess higher core energies.

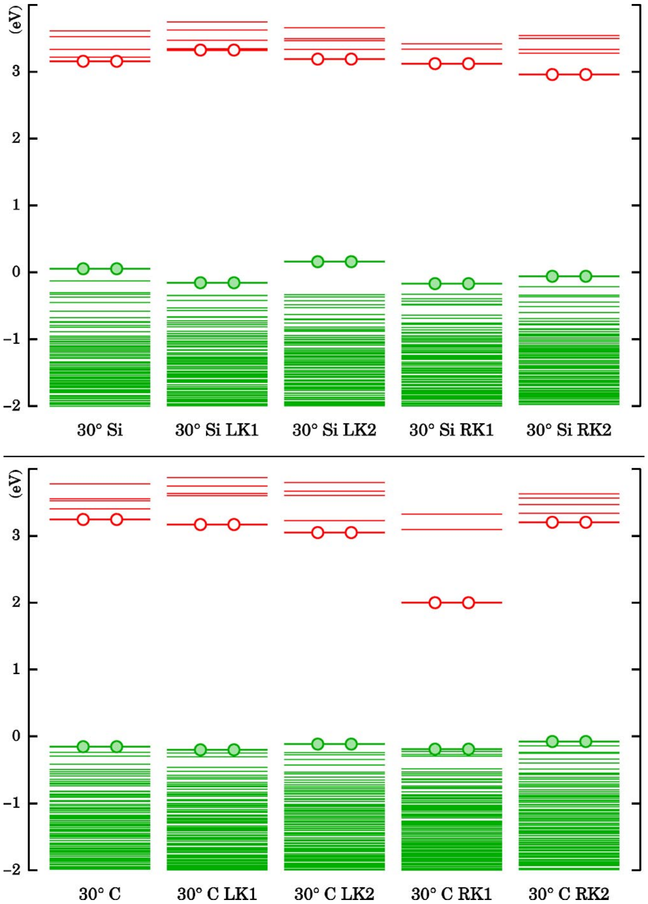

FIG. 10. The Kohn-Sham eigenvalue spectra of kinked 30° Shockley partials in SiC. The highest occupied and the lowest unoccupied states are indicated by two filled and two empty circles, respectively. As some of these states are localized gap levels (see text), they do not necessarily represent the valence-band maximum or the conduction-band minimum. The spectra are unscaled and energy zero is chosen arbitrarily through a shift constant for all structures. *Upper panel:* Si-terminated partial. *Lower panel:* C-terminated partial. The far left spectra give the respective unkinked partial.

In addition, the results strongly indicate that for all partials both energy and local structure are almost entirely independent of the polytype. Thus similar results can be expected for $4H$ and $6H$-SiC.

Like diamond and in contrast with silicon, the double-period 90° partials are about 90–100 meV/Å lower in energy than the single-period forms. Thus the smallest double-period partial is about 0.6 eV lower than a single-period one of the same length.

The electronic band structures of the straight partials were calculated both in $3C$- and $2H$-SiC. In both polytypes only the Si partials possess a relatively deep occupied band located about 0.4 eV above the VBM. These bands originate from the Si-Si reconstruction bonds. In contrast to this, the C partials do not lead to deep gap states.

Independent of the type of partial, the $2H$ polytype introduces additional empty bands below the CBM. These bands overlap those associated with the intrinsic stacking fault accompanying the partial dislocation and reach ≈ 0.5–0.6 eV into the gap. Due to the smaller gap, for $4H$- and $6H$-SiC one would expect the stacking fault bands to be closer to the conduction band, and indeed theoretical investigations by Miao *et al.*[12] for $4H$ and Iwata *et al.*[13] for $6H$ predict similar bands at 0.3 and 0.2 eV below the CBM, respectively. Except for the presence and positions of the stacking fault related bands the different polytypes seem to have no further influence on the electronic structure of the basal plane partials.

The glide motion of the four different Shockley partials—30° and 90° (SP), both Si and C terminated—has been considered as a process of kink formation and subsequent migration. Experimental results in $6H$-SiC give activation energies in a rather wide range of $Q = 2.1$–4.8 eV.[51,52] This is close to the range of activation energies found in this work, which range from 2.3 eV for the carbon-terminated 90° partial to 4.1 eV for the silicon-terminated 30° partial—assuming the glide process to involve the motion of long dislocation segments.

Overall, the 90° partial was found to be the more mobile species. Further, at least in the absence of strong obstacles, the mobility of carbon-terminated partials is significantly higher than silicon partials. The finding that the carbon partial is the mobile partial is in contradiction with the conclusions of Pirouz and Yang[53] where electron microscopy in $3C$-SiC was used to determine the identity of mobile partials by large-angle convergent beam electron-diffraction experiments.[54] This suggests that obstacles, e.g., impurities or radiation induced defects, may play an important role in pinning carbon partials. For example, nitrogen is a common impurity which is found exclusively at carbon sites. In this case glide is not controlled by the migration of kinks, but by the barrier to separate the kink from the obstacle.

Out of the ten elementary kinks, only three appear to introduce additional states in the gap: the high-energy left kink (LK2) at the 30° Si partial gives an occupied level ~ 0.4 eV above the VBM. At the C partial, the same kink (LK2) re-

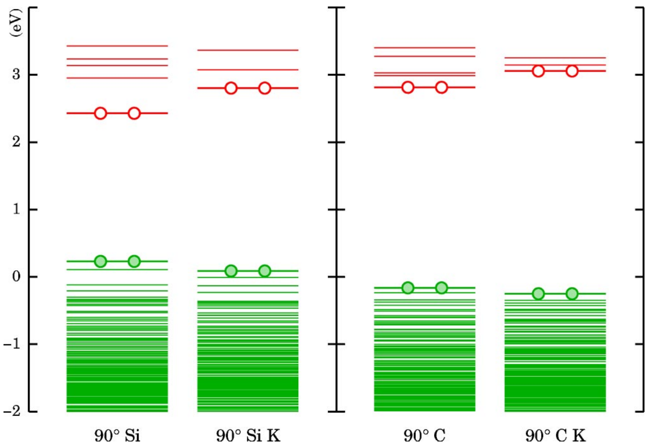

FIG. 11. The Kohn-Sham eigenvalue spectra of kinked 90° Shockley partials in SiC. For further details see caption of Fig. 10. *Left pair:* Si-terminated partial. *Right pair:* C-terminated partial. The left spectrum in each pair gives the respective unkinked partial.

constructs with a Si-Si bond and in a manner similar to Si-Si bonds in all Si partials, this leads to a localized level above the VBM. Finally, the low-energy right kink (RK1) at the 30° C partial gives rise to an empty level in the upper half of the band gap. In contrast to the 30° partials, all kinks at the 90° partials were found to be electrically inert.

Recombination-enhanced dislocation glide. As referred to above, the rapid degradation under forward-biased operation is a major problem in bipolar SiC device technology. In this irreversible process, stacking faults bounded by Shockley partials expand, introducing recombination centers and render the device useless. Neither the temperature nor the stress in these devices is sufficient to overcome the barriers for dislocation glide. Therefore, it is commonly believed that the bounding Shockley partials move by a recombination-enhanced dislocation glide (REDG), where the glide activation energy is substantially lowered by energy from nonradiative recombination at the dislocation core. So far the origin of the states participating in the nonradiative recombination process remains obscure. However, there are several important experimental findings, which have an impact on the question.

(1) In 4H-SiC, electroluminescence experiments by Galeckas *et al.*[6] reveal a 2.8-eV band involved in the degradation process. This recombination has been attributed to electronic bands induced by the fault at 0.2–0.6 eV below the conduction-band minimum, which were predicted by Iwata *et al.*,[14,13] Miao *et al.*,[12] and also in this work.

(2) Under forward bias a ∼1.8 eV electroluminescent band is found at mobile Shockley partials bordering the growing stacking faults.[6]

(3) Skowronski *et al.*[55] observed 30° partials in 4H-SiC moving under forward bias. In their experiments, light emission of considerable intensity as well as glide motion appeared to be restricted to one species of 30° partial only.

(4) The activation energy for the movement of the 30° partial under forward bias is found to be 0.27 eV.[6] Comparing this with similar experimental estimates without bias, the authors of Ref. 6 suggest a nonradiative recombination trap ∼2.2 eV from one of the band edges at the Shockley partial to be responsible for the REDG mechanism. The 2.2 eV recombination energy then added to 0.27 eV then equals the activation energy of around 2.5 eV found from the temperature dependence of the yield stress.

We have shown here that the main difference between Si and C partials in terms of electronic structure appears to be the presence of states 0.4 eV above the VBM in the case of Si partials. This, in combination with the aforementioned experimental findings, points towards a nonradiative recombination process between the gap states of the Si-terminated partials and those induced by the stacking fault. Assuming the latter states to be around 0.3 eV below the CBM (Ref. 12) together with a gap of 3.3 eV, and the states of the Si partials to be 0.4 eV above the VBM (this work), gives an estimate of 2.6 eV for the nonradiative recombination. Considering the band-gap error in DFT, this is in reasonable agreement with the 2.2 eV suggested in Ref. 6. It further suggests that only one type of partial—the Si partial which possesses electrical activity—is highly mobile under forward-bias, in contrast with the C partial. The latter, however, is the more mobile partial at high temperatures as it possesses lower glide activation energies (Tables VI and VII). The theory then is consistent with experiment as far as different partials are responsible for the REDG and high-temperature glide, but in conflict over the identity of the partials.

The origin of the 1.8-eV emission associated with the mobile partials remains unclear. It cannot be explained by the electronic gap states found for the straight partial or the kinks. The 1.8-eV emission could, however, be related to intrinsic defects such as Si vacancies which are trapped at the dislocation cores. The Si vacancy in 4H-SiC has internal emission lines at 1.458 and 1.352 eV,[56] but internal recombination from higher excitations (around 1.8 eV above the ground state) could occur in the vicinity of a dislocation. However, further studies are needed to resolve these issues.

---

*Email address: blumenau@phys.upb.de

[1] W.V. Münch, in *Numerical Data and Functional Relationships in Science and Technology*, edited by O. Madelung, Landolt-Börnstein, New Series, Group III, Vol. 17, Pt. a (Springer, Berlin, 1982), Chap. 1.5.

[2] O. Kordina, J.P. Bergman, A. Henry, E. Janzén, S. Savage, J. André, L.P. Ramberg, U. Lindefelt, W. Hermansson, and K. Bergman, Appl. Phys. Lett. **67**, 1561 (1995).

[3] H. Lendenmann, F. Dahlquist, N. Johansson, R. Söderholm, P.Å. Nilsson, J.P. Bergman, and P. Skytt, Mater. Sci. Forum **353–356**, 727 (2000).

[4] A. Galeckas, J. Linnros, B. Breitholtz, and H. Bleichner, Mater. Sci. Forum **353–356**, 389 (2000).

[5] J.P. Bergman, H. Lendenmann, P.Å. Nilsson, U. Lindefelt, and P. Skytt, Mater. Sci. Forum **353–356**, 299 (2000).

[6] A. Galeckas, J. Linnros, and P. Pirouz, Appl. Phys. Lett. **81**, 883 (2002).

[7] J.Q. Liu, M. Skowronski, C. Hallin, R. Söderholm, and H. Len-

denmann, Appl. Phys. Lett. **80**, 749 (2002).

[8] P.O.Å. Persson, L. Hultman, H. Jacobson, J.P. Bergman, E. Janzén, J.M. Molina-Aldareguia, W.J. Clegg, and T. Tuomi, Appl. Phys. Lett. **80**, 4852 (2002).

[9] J.D. Weeks, J.C. Tully, and L.C. Kimerling, Phys. Rev. B **12**, 3286 (1975).

[10] H. Sumi, Phys. Rev. B **29**, 4616 (1984).

[11] K. Maeda and S. Takeuchi, in *Dislocations in Solids*, edited by F.R.N. Nabarro and M.S. Duesbery (North-Holland, Amsterdam, 1996), Vol. 10, p. 444.

[12] M.S. Miao, S. Limpijumnong, and W.R.L. Lambrecht, Appl. Phys. Lett. **79**, 4360 (2001).

[13] H. Iwata, U. Lindefelt, S. Öberg, and P.R. Briddon, Phys. Rev. B **65**, 033203 (2002).

[14] H. Iwata, U. Lindefelt, S. Öberg, and P.R. Briddon, Mater. Sci. Forum **529**, 389 (2002).

[15] J.-L. Demenet, M.H. Hong, and P. Pirouz, Scr. Mater. **43**, 865 (2000).

[16] M. Zhang, H.M. Hobgood, J.-L. Demenet, and P. Pirouz, Mater. Sci. Forum **389**, 767 (2002).

[17] P.K. Sitch, R. Jones, S. Öberg, and M.I. Heggie, Phys. Rev. B **52**, 4951 (1995).

[18] A.T. Blumenau, C.J. Fall, R. Jones, M.I. Heggie, P.R. Briddon, T. Frauenheim, and S. Öberg, J. Phys.: Condens. Matter **14**, 12 741 (2002).

[19] D. Porezag, T. Frauenheim, T. Köhler, G. Seifert, and R. Kaschner, Phys. Rev. B **51**, 12 947 (1995).

[20] T. Frauenheim, G. Seifert, M. Elstner, Z. Hajnal, G. Jungnickel, D. Porezag, S. Suhai, and R. Scholz, Phys. Status Solidi B **217**, 41 (2000).

[21] A.T. Blumenau, M.I. Heggie, C.J. Fall, R. Jones, and T. Frauenheim, Phys. Rev. B **65**, 205205 (2002).

[22] C.J. Fall, A.T. Blumenau, R. Jones, P.R. Briddon, T. Frauenheim, A. Gutiérrez-Sosa, U. Bangert, A.E. Mora, J.W. Steeds, and J.E. Butler, Phys. Rev. B **65**, 205206 (2002).

[23] R. Jones and P.R. Briddon, in *Identification of Defects in Semiconductors*, edited by M. Stavola, Semiconductors and Semimetals Vol. 51A (Academic Press, Bristol, Boston, MA, 1998), Chap. 6.

[24] P. Briddon and R. Jones, Phys. Status Solidi B **217**, 131 (2000).

[25] X. Blase, K. Lin, A. Canning, S.G. Louie, and D.C. Chrzan, Phys. Rev. Lett. **84**, 5780 (2000).

[26] G.B. Bachelet, D.R. Hamann, and M. Schlüter, Phys. Rev. B **26**, 4199 (1982).

[27] H.J. Monkhorst and J.D. Pack, Phys. Rev. B **13**, 5188 (1976).

[28] W. Voigt, *Lehrbuch der Kristallphysik* (Teubner, Leipzig, 1928).

[29] J.P. Hirth and J. Lothe, *Theory of Dislocations*, 2nd ed. (Wiley, New York, 1982).

[30] J. Tersoff, Phys. Rev. B **39**, 5566 (1989).

[31] D.H. Lee and J.D. Joannopoulos, Phys. Rev. Lett. **48**, 1846 (1982).

[32] W.R.L. Lambrecht, B. Segall, M. Methfessel, and M. van Schilfgaarde, Phys. Rev. B **44**, 3685 (1991).

[33] A.P. Mirgorodsky, M.B. Smirnov, E. Abdelmounîm, T. Merle, and P.E. Quintard, Phys. Rev. B **52**, 3993 (1995).

[34] R.D. Carnahan, J. Am. Ceram. Soc. **51**, 223 (1968).

[35] D.W. Feldman, J.H. Parker, Jr., W.J. Choyke, and L. Patrick, Phys. Rev. **173**, 787 (1968).

[36] G. Arlt and G.R. Schodder, J. Acoust. Soc. Am. **37**, 384 (1965).

[37] S. Karmann, R. Helbig, and R.A. Stein, J. Appl. Phys. **66**, 3922 (1989).

[38] K. Kamitani, M. Grimsditch, J.C. Nipko, C.-K. Loong, M. Okada, and I. Kimura, J. Appl. Phys. **82**, 3152 (1997).

[39] J. Bennetto, R.W. Nunes, and D. Vanderbilt, Phys. Rev. Lett. **79**, 245 (1997).

[40] R.W. Nunes and D. Vanderbilt, J. Phys.: Condens. Matter **12**, 10 021 (2000).

[41] L.J. Teutonico, Phys. Rev. **124**, 1039 (1961).

[42] L.J. Teutonico, Phys. Rev. **127**, 413 (1962).

[43] O. Kubaschewski and C.B. Alcock, *Metallurgical Thermochemistry* (Pergamon, Oxford, 1979).

[44] K. Maeda, K. Suzuki, S. Fujita, M. Ishihara, and S. Hyodo, Philos. Mag. A **57**, 573 (1988).

[45] M.H. Hong, A.V. Samant, and P. Pirouz, Philos. Mag. A **80**, 919 (2000).

[46] P. Käckell, J. Furthmüller, and F. Bechstedt, Phys. Rev. B **58**, 1326 (1998).

[47] M. Kaukonen, P.K. Sitch, G. Jungnickel, R.M. Nieminen, S. Pöykkö, D. Porezag, and T. Frauenheim, Phys. Rev. B **57**, 9965 (1998).

[48] R.W. Nunes, J. Bennetto, and D. Vanderbilt, Phys. Rev. B **57**, 10 388 (1998).

[49] E. Rauls, Ph.D. thesis, Faculty of Science, Department of Physics, Universität Paderborn, 2003.

[50] E. Rauls, A. Gali, P. Deák, and T. Frauenheim, Phys. Rev. B **68**, 155208 (2003).

[51] S. Fujita, K. Maeda, and S. Hyodo, Philos. Mag. A **55**, 203 (1987).

[52] A.V. Samant, W.L. Zhou, and P. Pirouz, Phys. Status Solidi A **166**, 155 (1998).

[53] P. Pirouz and J.W. Yang, Ultramicroscopy **51**, 189 (1993).

[54] X.J. Ning and P. Pirouz, Inst. Phys. Conf. Ser. **142**, 449 (1996).

[55] M. Skowronski, J.Q. Liu, W.M. Vetter, M. Dudley, C. Hallin, and H. Lendenmann, J. Appl. Phys. **92**, 4699 (2002).

[56] E. Sörmann, N.T. Son, W.M. Chen, O. Kordina, C. Hallin, and E. Janzén, Phys. Rev. B **61**, 2613 (2000).

[57] Possible glide planes in $4H$ and $6H$ are locally embedded in cubic stacking of the nearest and next-nearest planes on one side and hexagonal stacking on the other. Further in $6H$, glide planes with locally cubic stacking on both sides are possible.